Nanoscale Advances

ROYAL SOCIETY OF CHEMISTRY

PAPER

View Article Online
View Journal | View Issue

Cite this: *Nanoscale Adv.*, 2022, **4**, 3083

Structural modification of salt-promoted MgO sorbents for intermediate temperature CO_2 capture†

Dasol Choi [a] and Youngjune Park *[ab]

MgO-based sorbents are a promising option for CO_2 capture at intermediate temperatures. MgO-based sorbents are often hybridized with alkali metal salts to promote the CO_2 capture performance. However, MgO-based sorbents often suffer a rapid decrement of CO_2 capture performance during multicycle carbonation–calcination reactions due to the reduction of active sites. In this study, we attempted to enhance the durability of MgO-based sorbents by modifying their morphology. A tubular-shaped MgO-based sorbent was synthesized using a carbon nanotube template. Various characterization experiments and evaluations were performed with the synthesized MgO-based materials. The MgO sample with modified structure exhibited a specific morphology consisting of elongated plate-like structures separated by empty spaces. This separation is expected to prevent MgO agglomeration and preserve the modified morphology during iterative CO_2 capture reactions. The MgO with modified structure achieved higher cycling stability with four times slower performance decay than the control MgO, even though identical chemical compositions were applied.

Received 5th April 2022
Accepted 9th June 2022

DOI: 10.1039/d2na00213b

rsc.li/nanoscale-advances

Introduction

In response to the steeply rising demand for CO_2 reduction, CO_2 capture, utilization, and storage (CCUS) techniques are being intensively studied for various CO_2 emission conditions.[1,2] In particular, CO_2 emissions at intermediate temperatures (*i.e.*, 200–400 °C) are important CCUS targets that include post-combustion flue gas, CO_2/H_2 separation after the water–gas shift reaction, and the steam reforming reaction of methanol.[3–5] Chemical adsorption of CO_2 on solid MgO is considered a suitable option for CO_2 capture at intermediate temperatures, which is based on the reversible carbonation–calcination reaction of MgO–$MgCO_3$ (*i.e.*, MgO (s) + CO_2 (g) ⇌ $MgCO_3$ (s)) at working temperatures of 250–400 °C.[6–8] Solid MgO directly captures CO_2 from gas streams to form $MgCO_3$, and the regeneration can be easily performed by heating the $MgCO_3$ beyond 400 °C to produce MgO and a CO_2-enriched stream.[8] This process has the distinct advantage of high theoretical CO_2 capture capacity (24.8 mol CO_2 per kg MgO). Furthermore, the energy requirement for regeneration can be moderated by heat recovery from the exothermic CO_2 capture step at 350 °C.[9]

To apply MgO-based sorbents to the CO_2 capture process, further enhancements of CO_2 capture performance and durability must be achieved. The gas–solid reaction between MgO and CO_2 often suffers from the low conversion of MgO to $MgCO_3$ due to the stable lattice structure of Mg^{2+}–O^{2-} and the passivation of unreacted inner MgO by $MgCO_3$ on the surface at the initial stage of carbonation.[7,10] Salt-promoted MgO carbonation has been intensively studied by applying mixtures of various alkali nitrate salts and alkali carbonate salts, which can significantly enhance the overall MgO carbonation efficiency.[11–15] For example, it was reported that the salt mixture $2(Li_{0.44}K_{0.56})NO_3/(Na_{0.5}K_{0.5})_2CO_3$ exhibits highly improved CO_2 capture performance.[16,17]

Enhancing the durability of MgO-based sorbents is another challenge. Even though high performance MgO-based sorbents can be achieved by salt-promotion, a rapid decrement of recyclability is often observed during multicycle carbonation–calcination reactions due to the reduction of active sites by agglomeration of MgO particles.[13,15,16,18–20] Sintering of $MgCO_3$ is considered a principal factor that provokes agglomeration, which is caused by the low Tammann temperature of $MgCO_3$ and accelerated atomic diffusion at the interface between $MgCO_3$ and the molten salt promoter.[16,18,21] In addition, the chemisorption of CO_2 can cause the expansion of MgO particle volume due to the density difference between MgO and $MgCO_3$. Therefore, it is thought that the volume expansion of particles

[a]*School of Earth Sciences and Environmental Engineering, Gwangju Institute of Science and Technology (GIST), 123 Cheomdangwagi-ro, Buk-gu, Gwangju 61005, Republic of Korea. E-mail: young@gist.ac.kr*

[b]*Research Center for Innovative Energy and Carbon Optimized Synthesis for Chemicals (Inn-ECOSysChem), Gwangju Institute of Science and Technology (GIST), 123 Cheomdangwagi-ro, Buk-gu, Gwangju 61005, Republic of Korea*

† Electronic supplementary information (ESI) available. See https://doi.org/10.1039/d2na00213b

accelerates agglomeration and blocks small pores, resulting in a reduction of active sites available for the reversible reaction.

This study aims to enhance the durability of MgO-based sorbents in the reversible carbonation–calcination reaction by modifying the morphology to preserve active sites. For this, tubular-shaped MgO particles were synthesized to restrain grain overlapping by producing inner empty spaces. In order to produce tubular MgO particles, multi-walled carbon nanotubes (CNT) were used as a template for the precipitated $MgCO_3$. Two samples were prepared, one by removing and one by retaining the CNT template, and their reaction behaviors were compared. The prepared MgO sorbents were characterized *via* Raman, XRD, TGA, and BET analyses, and morphology evolution during the multicycle reaction was observed by SEM and TEM. The relationship between controlled morphology and multicycle CO_2 capture performance was discussed.

Experimental

Materials

Magnesium chloride ($MgCl_2$, 98%), multi-walled carbon nanotubes (CNT, >90% carbon basis, $D = 110$–170 nm, $L = 5$–9 μm), lithium nitrate ($LiNO_3$, 99%), potassium nitrate (KNO_3, 99%), sodium carbonate (Na_2CO_3, 99%), potassium carbonate (K_2CO_3, 99%), hydrochloric acid (HCl, 99%), and nitric acid (HNO_3, 99%) were purchased from Sigma-Aldrich Co. (USA). N_2 gas and CO_2 gas were supplied by Shinil Gas Co., Ltd (Republic of Korea).

Preparation of MgO/CNT sorbents

The synthesis method of MgO precipitated on the CNT template was modified by referring to the literature.[22,23] As the alkali metal salt (AMS) promoter, a hybrid salt of nitrate and carbonate, $2(Li_{0.44}K_{0.56})NO_3/(Na_{0.5}K_{0.5})_2CO_3$, was employed for carbonation enhancement.[16,17] Three types of MgO-based sorbents, MgO/CNT_N_2, MgO/CNT_Air, and MgO, were synthesized. MgO/CNT_N_2 was a MgO-based sorbent on a CNT template. MgO/CNT_Air was a MgO-based sorbent on a sacrificial CNT template that was thermally removed afterward. The control sample MgO was prepared without CNT but in the same manner. The samples are listed in Table 1. The ratio of AMS promoter to MgO was determined according to the referenced studies.[16,17]

CNT activation. In order to purify and activate CNT, reagent CNT was treated with strong acid. 100 mL of 5 M HNO_3 and 5 M HCl solution was prepared by mixing 36 mL of HCl, 22 mL of HNO_3, and 42 mL of deionized water. Then 0.500 g of CNT was added to the acid solution. The CNT-added solution was sonicated for 30 min, stirred with a magnetic bar at 300 rpm for 2 h, and aged for 24 h at room temperature. Treated CNT was filtered, washed with deionized water, and dried at 120 °C for 2 h in a muffle furnace with a ramping rate of 3 K min^{-1}.

Precipitation on the CNT templates. In order to form tubular-shaped morphology, $MgCO_3$ particles were precipitated on the activated CNT. 40 mg of activated CNT was dispersed in 40 mL of deionized water by sonication. 1.382 g of K_2CO_3 was dissolved in 20 mL of deionized water, followed by mixing with CNT solution at 50 °C *via* 300 rpm magnetic stirring. $MgCl_2$ solution was prepared by dissolving 0.952 g of $MgCl_2$ in 40 mL of deionized water. $MgCl_2$ solution was added dropwise to the CNT/K_2CO_3 solution and reacted for 24 h at 50 °C *via* 300 rpm magnetic stirring. The obtained $MgCO_3$/CNT powder was filtered and washed with deionized water. Then it was dried in a convection oven at 60 °C for 12 h. The $MgCO_3$ control sample was precipitated using 60 mL of 1.382 g K_2CO_3 solution and 40 mL of 0.952 g $MgCl_2$ solution. $MgCl_2$ solution was added dropwise to the K_2CO_3 solution and reacted for 24 h at 50 °C *via* 300 rpm magnetic stirring. The obtained $MgCO_3$ powder was filtered and washed with deionized water. Then it was dried in a convection oven at 60 °C for 12 h.

Thermal treatment. The prepared $MgCO_3$ samples were thermally decomposed to MgO using a tube furnace. For MgO/CNT_N_2, the $MgCO_3$ in the $MgCO_3$/CNT powder was thermally decomposed to MgO at 450 °C for 2 h in a tube furnace purged with N_2 gas. For MgO/CNT_Air, the $MgCO_3$ and CNT in the $MgCO_3$/CNT powder were thermally decomposed to MgO at 450 °C for 2 h in a tube furnace purged with air. For the MgO control sample, the prepared $MgCO_3$ was thermally decomposed at 450 °C for 2 h in a tube furnace purged with N_2 gas. The resulting MgO samples were then gently ground with a mortar and pestle.

Salt impregnation. $2(Li_{0.44}K_{0.56})NO_3/(Na_{0.5}K_{0.5})_2CO_3$ was impregnated as an AMS additive into the prepared MgO samples. To 150 mL of methanol, 0.33 mmol of $LiNO_3$, 0.42 mmol of KNO_3, 0.1875 mmol of Na_2CO_3, and 0.1875 mmol of K_2CO_3 were added. The salt solution was sonicated for 2 h and then stirred with a magnetic bar at 300 rpm for 18 h. To the 50 mL of salt solution, 0.1 g of the prepared MgO/CNT or MgO was added. The solution was sonicated for 2 h and mixed *via* 300 rpm magnetic stirring for 18 h. Then solution was evaporated at 50 °C for 3 h. The obtained salt-impregnated MgO samples were gently ground with a mortar and pestle.

Table 1 List of samples

	Composition (wt%)		
Sample notation	MgO	AMS	CNT
MgO/CNT_N_2	68	25	7
MgO/CNT_Air	73	27	—
MgO	73	27	—

Characterization

In order to characterize the prepared MgO samples, a powder X-ray diffractometer (XRD, SmartLab, Rigaku Corp., Japan) with Cu K_α (1.54 Å) radiation, and a dispersive Raman spectrometer (iHR-SP320, Horiba Jobin Yvon Inc., France) were employed. The dispersive Raman spectrometer was coupled with a diode-pumped CW laser with a wavelength of 543 nm, charge-coupled device (CCD) detector, and 1800 groove per mm grating. In order to identify the morphology of the prepared MgO samples, a field emission-scanning electron microscope

(FE-SEM, S-4700, Hitachi Ltd, Japan) and scanning transmission electron microscope-energy dispersive spectrometer (STEM-EDX, Tecnai G2 F30 S-Twin, FEI, USA) were employed. In order to identify the structural properties, Brunauer–Emmett–Teller (BET) surface area analysis and Barrett–Joyner–Halenda (BJH) pore size distribution analysis were performed using a surface area and pore size analyzer (3Flex, Micromeritics, USA). Density was measured by a He gas pycnometer (AccuPyc II 1340, Micromeritics, USA).

Iterative CO_2 capture analysis

In order to obtain the CO_2 capture performance of MgO samples, thermogravimetric analysis (TGA) and differential scanning calorimetry (TGA-DSC, LABSYS EVO STA, Setaram Inc., France) were performed. For each measurement, an ~10 mg sample was placed into a ceramic crucible. Iterative carbonation–calcination reactions were performed for 30 cycles and 100 cycles (MgO/CNT_Air) using a ramping rate of 10 K min^{-1}. For the carbonation of MgO to $MgCO_3$, a CO_2 gas flow was applied at 350 °C for 1 h. For the calcination of $MgCO_3$ to MgO, N_2 gas was applied at 400 °C for 1 h. The MgO sample was tested under an additional condition for complete calcination, referred to as MgO_HT. In this case, N_2 gas was applied at a higher temperature of 450 °C for 1 h. In order to prepare the BET samples of MgO and MgO/CNT_Air after cyclic reaction, the iterative reactions were performed using a tube furnace and TGA under CO_2 gas at 350 °C, 1 h for carbonation, and 500 °C, 5 min for calcination. The conversion of MgO to $MgCO_3$ at the N^{th} cycle (X_N) was calculated using the weight difference before and after carbonation at each cycle.

$$\text{MgO conversion, } X_N = \frac{N_{MgCO_3}}{N_{MgO}} = \frac{\text{weight difference at the } N^{th} \text{ cycle/molar mass of } CO_2}{\text{weight of pristine MgO/molar mass of MgO}} \quad (1)$$

Results and discussion

Characterization before the multicycle reaction

To produce tubular-shaped MgO, precipitation of MgO on the CNT template was performed. During the synthesis, two types of MgO/CNT samples were prepared. The MgO/CNT_N_2 sample was calcined under N_2; the resulting sample is expected to contain CNT. The MgO/CNT_Air sample was calcined under air; the resulting sample is expected to contain no residual CNT. Raman spectra were obtained for the characterization of chemicals in the prepared samples. For morphology characterization, SEM and TEM were employed.

Raman spectra of the prepared MgO-based samples are shown in Fig. 1. AMS peaks were observed in all MgO samples representing the ν_4 asymmetric bending modes of CO_3^{2-} and NO_3^{2-} ions (both at 714 cm^{-1}), and ν_1 symmetric stretching mode of the CO_3^{2-} ion (~1050 cm^{-1}) and NO_3^{2-} ion (1091 cm^{-1}).[24] Clear peaks of CNT were observed in the MgO/CNT_N_2 sample. D band (1345 cm^{-1}), G band (1576 cm^{-1}), and G′ band (2690 cm^{-1}) peaks of CNT were observed.[25–27]

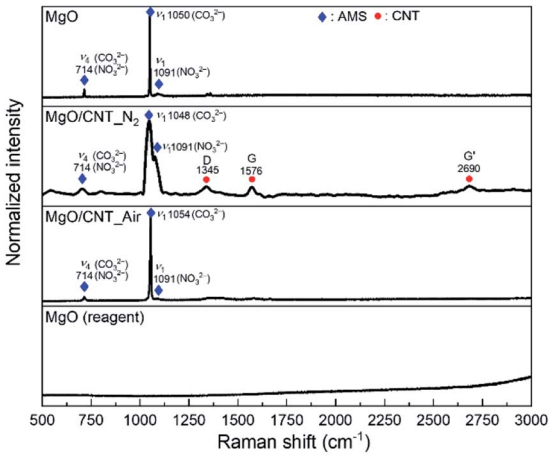

Fig. 1 Raman spectra of pristine MgO-based sorbents.

No CNT peak of the MgO/CNT_Air sample was detected in the Raman spectrum. The existence of residual CNT was double-checked by measuring the weight change of the MgO/CNT_Air sample during combustion, as shown in Fig. S1.† The result indicated that the residual CNT was almost negligible. The Raman spectroscopy results confirmed that the MgO-based sorbents were synthesized well according to the intended chemical composition design.

Morphologies of the prepared MgO-based samples were analyzed by SEM and TEM images, as shown in Fig. 2. Supplementary SEM and TEM images are also provided in Fig. S2.† In the SEM images (Fig. 2(a)–(c)), the morphologies of MgO/CNT_N_2 and MgO/CNT_Air samples were significantly different from those of the MgO sample. The MgO sample consisted of spherical MgO particles that were agglomerated with each other. However, spherical MgO particles had changed into MgO flakes in the MgO/CNT_N_2 and MgO/CNT_Air samples. In the TEM images (Fig. 2(d)–(f)), MgO/CNT_N_2 and MgO/CNT_Air samples exhibit tubular structures, in contrast to the structure of MgO. In the MgO/CNT_N_2 sample (Fig. 2(d)), hair-like structures were observed, which is supposed to be CNT. On the other hand, the MgO/CNT_Air sample (Fig. 2(e)) showed no hair-like structures. Elemental distributions on the surfaces of the samples were obtained by using EDX (Fig. S3†). The results particularly confirmed that the tubular structures of the MgO/CNT_Air sample consisted of MgO grains.

Iterative CO_2 capture behavior

The CO_2 capture performance of MgO-based sorbents during 30 cycles of carbonation–calcination was measured by TG-DSC, and the results are shown in Fig. 3. Weight profiles of MgO-based sorbents during carbonation (indicated as increments) and calcination (indicated as decrements) are shown in Fig. 3(a). MgO conversion (X_N) as a function of cycle number is given in Fig. 3(b). In Fig. 3(a), MgO-based sorbents exhibit different reaction patterns according to their weight profiles. The MgO/CNT_N_2 sample exhibited a continuous decrement of

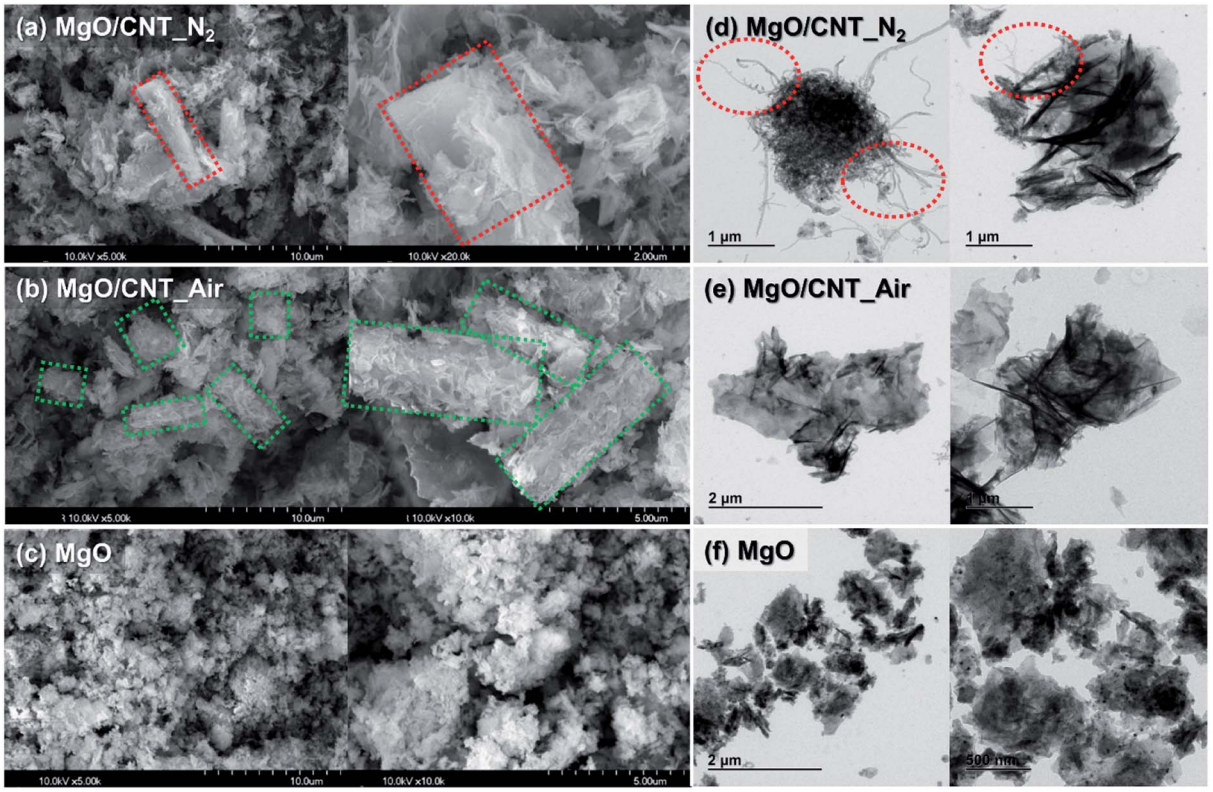

Fig. 2 SEM and TEM images of pristine MgO sorbents. SEM images of (a) MgO/CNT_N_2, (b) MgO/CNT_Air, and (c) MgO samples, and TEM images of (d) MgO/CNT_N_2, (e) MgO/CNT_Air, and (f) MgO. Dotted areas in red and in green indicate CNT with MgO flakes, and tubular-shaped MgO flakes without CNT, respectively.

calcined weight, particularly in the early stages, and then the carbonation–calcination reactions were almost inactivated. On the other hand, the MgO/CNT_Air sample exhibited more stable patterns in each cycle, although slightly fluctuating patterns occurred in the early cycles. The MgO sample exhibited quite different patterns from those of the other samples. The weights of the MgO sample after calcination continuously increased for the first 10 cycles and stabilized for further cycles. The incomplete calcination indicates that $MgCO_3$ was not fully regenerated to MgO, reducing the available MgO for the next CO_2 capture cycle. The reason for incomplete calcination can be found in the work of Maya *et al.*,[28] in the $CaCO_3$–CaO reaction system. They claimed the "die-off" phenomenon that the CO_2 catalyzed sintering of the product CaO layer on the particle surface causes covering of the inner $CaCO_3$ by surface CaO. The reaction pattern of the MgO sample follows the die-off

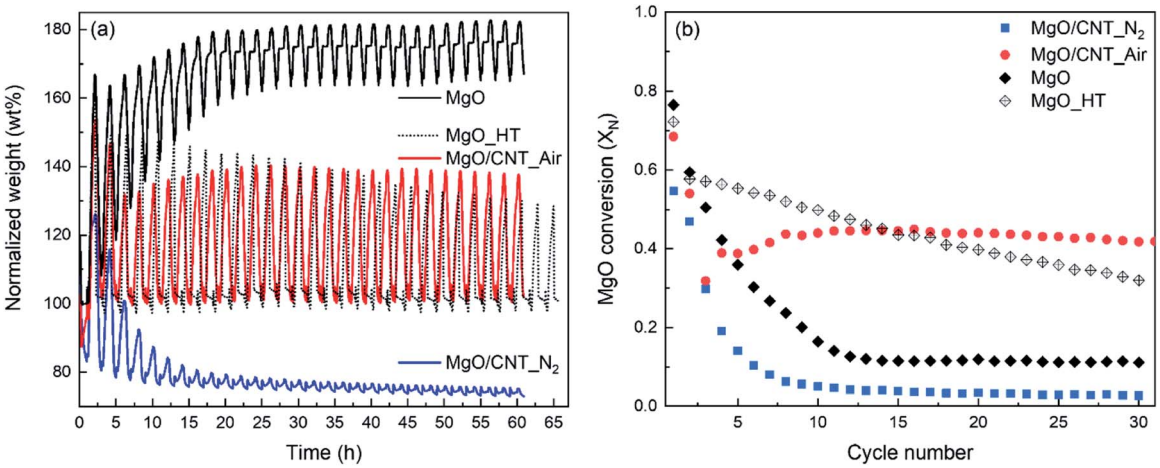

Fig. 3 CO_2 capture performance of MgO-based sorbents for 30 cycles of carbonation–dissociation measured by TG-DSC. (a) Normalized weight (wt%) profiles and (b) MgO conversion (X_N). Weight profiles are normalized according to each weight of pristine MgO-based sorbents.

phenomenon. In this situation, higher regeneration energy is required because the inner $MgCO_3$ layer requires energy for thermal decomposition and CO_2 escape through the surface MgO layer. The agglomerate-based morphology of the MgO sample might induce surface layer sintering for die-off. Interestingly, the multiple carbonation–calcination reactions of MgO/CNT_Air were relatively stable, particularly compared to the case of the MgO sample. This indicates that the modified morphology of MgO/CNT_Air possibly requires less regeneration energy. Note that the reaction conditions of the multiple carbonation–calcination were set identically for MgO, MgO/CNT_Air, and MgO/CNT_N_2.

The CO_2 capture performance of the MgO sample was examined again, applying a higher calcination reaction temperature of 450 °C to obtain complete regeneration (referred to as MgO_HT). As shown in Fig. 3(a), the MgO_HT sample exhibited stable carbonation and complete regeneration compared to the MgO sample. However, the degree of carbonation decreased continuously for the given cycles. Note that MgO/CNT_Air stably maintained its carbonation–calcination reactivity for the given period, even at the lower calcination temperature of 400 °C.

The weight change profiles of the above sample were converted to the MgO conversion (X_N) to $MgCO_3$, as shown in Fig. 3(b). MgO conversion of MgO/CNT_Air abruptly decreased from 0.68 (X_1) to 0.32 (X_3), then gradually increased to 0.39 (X_4) and 0.45 (X_{11}). After that, the conversion was stabilized at ~0.44 for the remaining cycles. The MgO sample similarly exhibited a steep decrement from 0.77 (X_1) to 0.12 (X_{13}). Then, the pattern stabilized with a low value of MgO conversion. On the other hand, MgO_HT exhibited a gradual decrease in MgO conversion from 0.58 (X_2) to 0.32 (X_{30}). Note that, starting from X_{15}, MgO/CNT_Air showed MgO conversion higher than that of MgO_HT. The recyclability of MgO/CNT_Air was further examined for 100 cycles of carbonation–calcination (Fig. 4). The MgO conversion of MgO/CNT_Air steadily decreased from 0.32 (X_{66}) to 0.26 (X_{100}). The decaying patterns of both MgO/CNT_Air and MgO_HT were analyzed. The slopes were −0.0023 (X_N/cycle) and −0.0095 (X_N/cycle) for MgO/CNT_Air and MgO_HT, respectively. These results indicate that the inactivation tendency of MgO_HT was four times faster than in the case of MgO/CNT_Air, which implies that MgO/CNT_Air can achieve better durability even under mild regeneration conditions.

Characterization after iterative reactions

The chemical natures of MgO-based sorbents were analyzed by Raman spectroscopy after 30 cycles of carbonation–calcination reactions (Fig. 5). The peak appearances of MgO and MgO/CNT_Air are identical throughout the multicycle reaction, as can be seen in Fig. 1. In MgO/CNT_N_2, the peaks at 714 cm^{-1} and 1091 cm^{-1}, representing the ν_4 asymmetric bending modes of CO_3^{2-} and NO_3^{2-} and ν_1 symmetric stretching mode of NO_3^{2-} ions, disappeared, respectively. In Fig. S5,† thermal decomposition of MgO/CNT_N_2 was validated by TG-DSC, representing the loss of AMS. Therefore, it is speculated that the decomposition of AMS occurred at the early stage of the multicycle reaction in the MgO/CNT_N_2 sample, which resulted in the rapid performance decay.

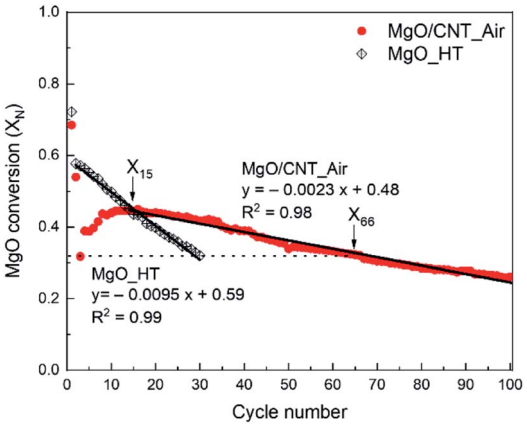

Fig. 4 CO_2 capture performance of MgO_HT (30 cycles) and MgO/CNT_Air (100 cycles) in MgO conversion (X_N) by TG-DSC. Linear regressions of performance decay are given.

SEM images were obtained to compare the evolution of the structure during the multicycle reaction of MgO/CNT_Air and MgO, with results shown in Fig. 6 and 7. Supplementary SEM images are also provided in Fig. S7 and S8.† Images in Fig. 6(a)–(c) show the alteration of MgO flakes into spherical particles. The carbonation into $MgCO_3$ induced a morphology of stacked rhombohedral plates with the trigonal crystal structure (Fig. 6(b)). The regeneration of $MgCO_3$ produced spherical particle-based MgO structures (Fig. 6(c)). Interestingly, the structure of regenerated MgO was affected by the pristine tubular structure. Each agglomeration of spherical MgO particles exhibited one-directional attachment, producing elongated plate-like structures. We assume that the wall of the tubular structure changed to an elongated plate-like structure, and the inner empty space of the tube produced the empty spaces. Elongated plate-like structures and empty spaces were repeatedly observed in the following iterative reactions. After 100 reaction cycles, the MgO/CNT_Air sample retained the

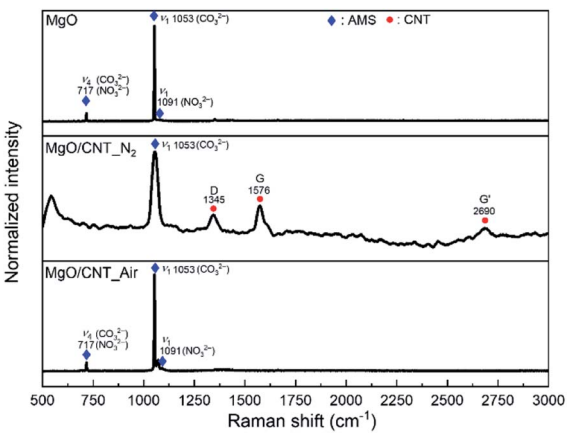

Fig. 5 Raman spectra of MgO-based sorbents after 30 cycles of carbonation–calcination reactions.

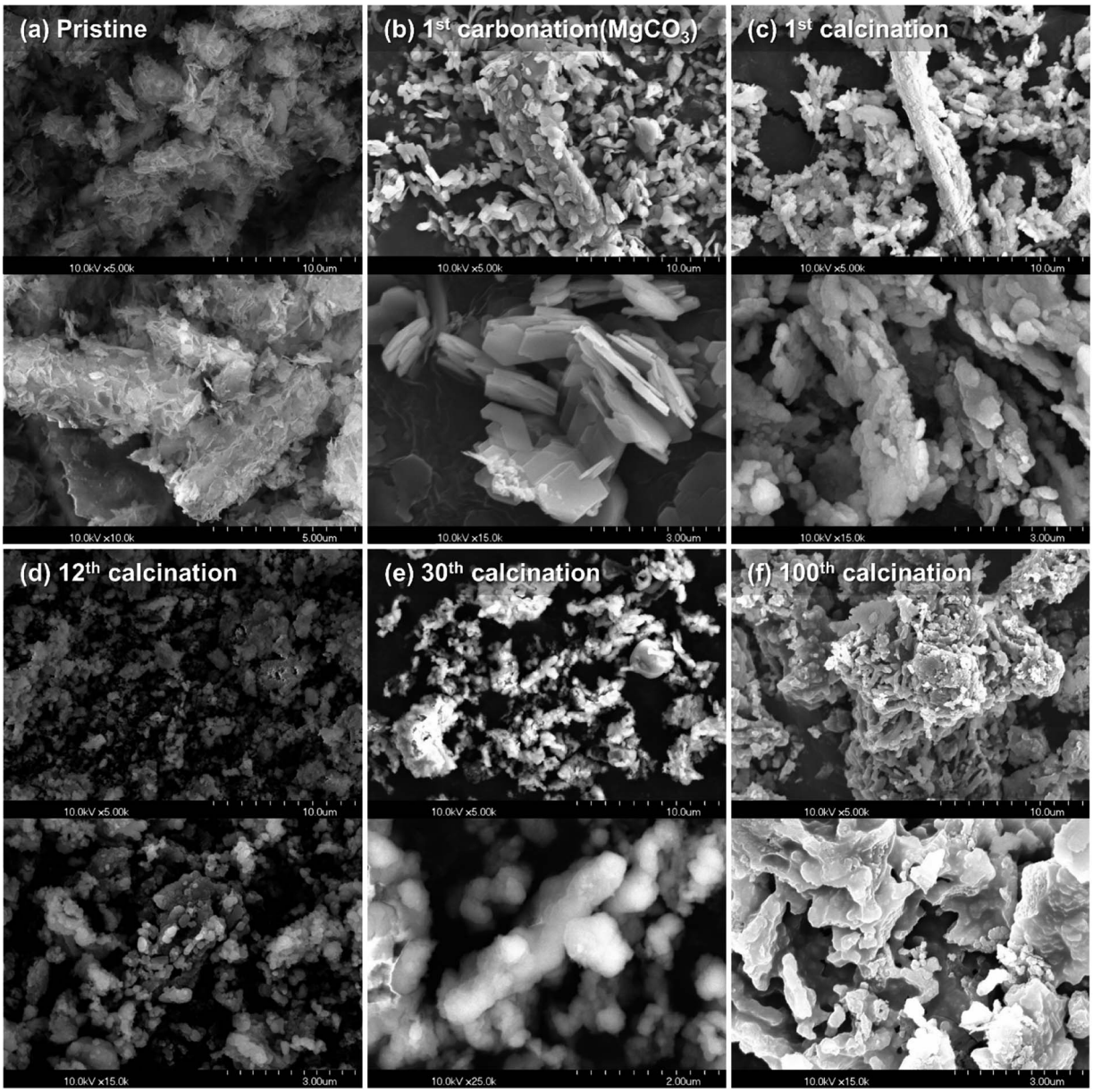

Fig. 6 SEM images of MgO/CNT_Air: (a) pristine, (b) 1st carbonation ($MgCO_3$), (c) 1st calcination, (d) 12th calcination, (e) 30th calcination, and (f) 100th calcination.

morphology of one-directional attachment of MgO particles and empty spaces, even though dense agglomerates were produced. In comparison, the MgO sample exhibited a non-directional agglomeration of spherical MgO particles (Fig. 7 and S8†). These agglomerates expanded during iterative reactions.

The BET surface area, BJH adsorption pore volume, pore diameter, pore distribution, and density were obtained with MgO/CNT_Air and MgO to compare the structural properties (Table 2). The analyses were performed after the first carbonation–calcination reaction to examine the adjusted morphology after the initial reaction (Fig. 6(b) and (c)). The results indicate that MgO/CNT_Air had lower surface area and pore volume than those characteristics of MgO in the initial stage. In pore size distribution (Fig. S9†), larger pores were predominantly observed in MgO/CNT_Air than in MgO. The structural properties can be explained by the elongated plate-like structure of MgO/CNT_Air, in which the rigid structure reduced the surface area, pore volume, and small pores. Despite the reduced surface area and pore volume, the density of MgO/CNT_Air was lower than that of MgO. The empty spaces can enlarge the material's volume and lower its density. Therefore, the obtained structural properties support the idea that the modified morphology of MgO/CNT_Air was an elongated plate-like structure with empty spaces.

The differences in structural properties indicate that MgO/CNT_Air had fewer active sites for CO_2 capture than MgO/CNT_Air in the initial cycle, which is consistent with the evaluation result of iterative CO_2 performance (Fig. 3). The

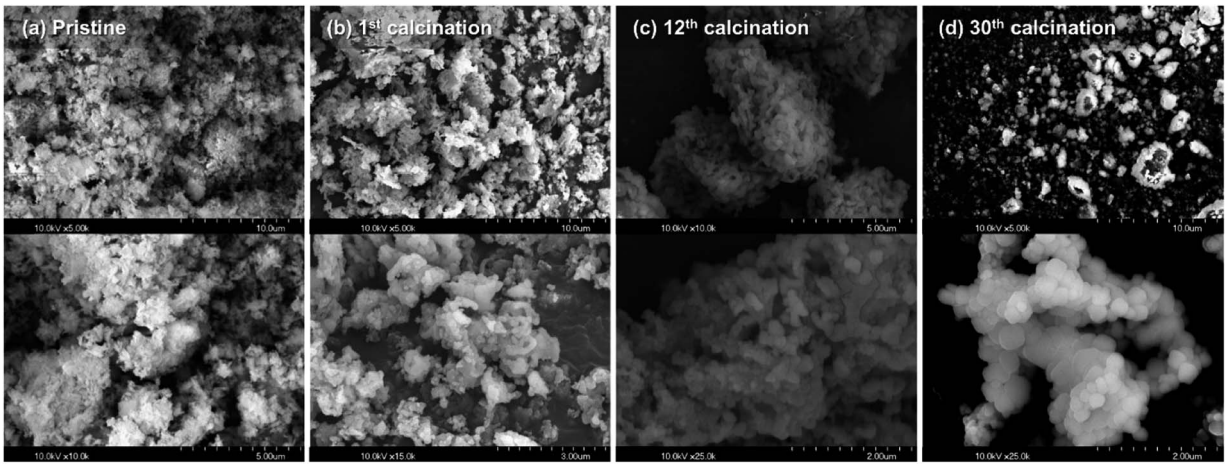

Fig. 7 SEM images of MgO: (a) pristine, (b) 1st calcination, (c) 12th calcination, and (d) 30th calcination.

structural properties after 30 cyclic reactions were obtained by performing cyclic reactions on BET samples using a tube furnace. The calcination reaction conditions were changed to 500 °C, 5 min under CO_2. These conditions were also employed when using TG-DSC, and the stable performance of MgO/CNT_Air and decreasing performance of MgO were re-confirmed (Fig. S10†). BET analysis results showed that the surface area and pore volume were reduced after 30 cycles. MgO exhibited a severe decrement in surface area and pore volume. The larger pores were also increased, which is evidence of sintering. MgO/CNT_Air also exhibited reduced surface area and pore volume, but the reduction was more moderate than MgO. The empty spaces might consume the large pores, and the average pore size became small. From the BET results, the modified morphology of MgO/CNT_Air effectively maintained the structural properties and delayed sintering.

Therefore, the MgO/CNT_Air with modified morphology exhibited enhanced cycling stability of CO_2 capture performance due to the delayed sintering. The modified morphology consists of elongated plate-like MgO structures separated by empty spaces. Sintering at the particle interfaces induces the agglomeration of particles and reduces active sites. The carbonation causes the volume expansion of particles, resulting in more interfaces. According to Bork *et al.*,[29] Gao *et al.*,[30] and Lee *et al.*,[31] the surface volume expansion from MgO to $MgCO_3$ was reported to be within hundreds of nanometers. However, the empty spaces in the modified morphology had a thickness of 1–2 μm. The empty spaces and plate-like structure could effectively reduce the intersection and agglomeration of separated MgO particles (Fig. 8). The agglomeration inhibition delayed the sintering of MgO/CNT_Air, resulting in extended durability. On the other hand, the morphology of MgO_HT had no inhibitory effect on agglomeration, resulting in gradual performance decay.

Structural modification of MgO-based sorbents is often focused on modifying the nanoscale structure of MgO. For example, mesoporous MgO,[18] nanosheet MgO,[16] nanostructured microsphere MgO,[32] and eggshell membrane template MgO[33] were proposed, achieving enhanced surface area and porosity. However, these MgO-based sorbents exhibited rapid performance decay in early cycles. Compared to other studies, the proposed MgO/CNT_Air has a unique decay pattern

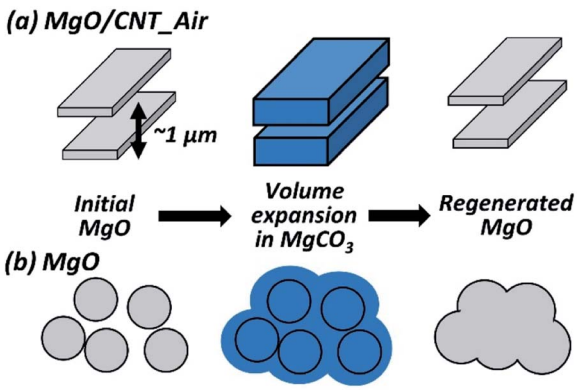

Fig. 8 Simplified schemes of morphological evolution during carbonation–calcination reaction in MgO/CNT_Air and MgO.

Table 2 BET analysis and density analysis of MgO and MgO/CNT_Air after the 1st and 30th carbonation–calcination reactions

	Cycle number	Surface area ($m^2\ g^{-1}$)	Pore volume ($cm^3\ g^{-1}$)	Average pore diameter (nm)	Density ($g\ cm^{-3}$)
MgO/CNT_Air	1	1.31	0.0085	49.48	2.64
	30	0.82	0.0063	14.57	
MgO	1	1.88	0.0132	32.37	2.72
	30	0.34	0.0075	62.74	

in which the CO_2 capture performance increased and was maintained in early cycles, allowing enhanced cycling stability. Therefore, the possibility of durability enhancement by micro-scale MgO structure modification is proposed for the first time.

Conclusions

Structural modification was performed by applying a multi-walled CNT as a template for MgO precipitation. A tubular-structured pristine MgO/CNT sample was synthesized, and the morphology evolved after the first carbonation–calcination into a unique modified morphology consisting of elongated plate-like MgO with empty spaces. The MgO control sample exhibited agglomeration of spherical MgO structures. Iterative CO_2 capture performance patterns were obtained by TG analysis. The MgO with modified structure achieved enhanced durability under milder regeneration conditions than those of the control group MgO, even though their chemical compositions were identical. Removal of CNT was required for enhanced performance because residual CNT induced decomposition of alkali metal salt promoters for gas–solid reaction. The modified morphology was preserved during iterative reactions because the empty spaces separated elongated plate-like MgO structures and prevented the agglomeration due to expanded volume through carbonation. The morphology preservation delayed the sintering of MgO structures, resulting in enhanced durability of the CO_2 capture performance.

Conflicts of interest

There are no conflicts to declare.

Acknowledgements

This research was supported by Korea Electric Power Corporation (grant number: R19XO01-07) and a National Research Foundation of Korea (NRF) grant funded by the Korean government (MSIT) (no. 2021R1A5A1028138).

References

1 J. H. Park, J. Yang, D. Kim, H. Gim, W. Y. Choi and J. W. Lee, *Chem. Eng. J.*, 2022, **427**, 130980.
2 J.-N. Kang, Y.-M. Wei, L.-c. Liu and J.-W. Wang, *Technol. Forecast. Soc. Change*, 2021, **171**, 120933.
3 A. I. Osman, M. Hefny, M. I. A. A. Maksoud, A. M. Elgarahy and D. W. Rooney, *Environ. Chem. Lett.*, 2021, **19**, 797–849.
4 S. Sun, H. Sun, P. T. Williams and C. Wu, *Sustainable Energy Fuels*, 2021, **5**, 4546–4559.
5 D. Jansen, M. Gazzani, G. Manzolini, E. v. Dijk and M. Carbo, *Int. J. Greenhouse Gas Control*, 2015, **40**, 167–187.
6 X. Yang, L. Zhao, X. Li and Y. Xiao, *Curr. Pollut. Rep.*, 2018, **4**, 13–22.
7 A. H. Ruhaimi, M. A. A. Aziz and A. A. Jalil, *J. CO2 Util.*, 2021, **43**, 101357.
8 J. Ding, C. Yu, J. Lu, X. Wei, W. Wang and G. Pan, *Appl. Energy*, 2020, **263**, 114681.
9 T. Papalas, I. Polychronidis, A. N. Antzaras and A. A. Lemonidou, *J. CO2 Util.*, 2021, **50**, 101605.
10 J. Fagerlund, J. Highfield and R. Zevenhoven, *RSC Adv.*, 2012, **2**, 10380–10393.
11 T. Harada, F. Simeon, E. Z. Hamad and T. A. Hatton, *Chem. Mater.*, 2015, **27**, 1943–1949.
12 G. Bang, K.-M. Kim, S. Jin and C.-H. Lee, *Chem. Eng. J.*, 2022, **433**, 134607.
13 J. Wang, M. Li, P. Lu, P. Ning and Q. Wang, *Chem. Eng. J.*, 2020, **392**, 123752.
14 T. Papalas, A. N. Antzaras and A. A. Lemonidou, *J. CO2 Util.*, 2021, **53**, 101725.
15 A.-T. Vu, K. Ho, S. Jin and C.-H. Lee, *Chem. Eng. J.*, 2016, **291**, 161–173.
16 L. Wang, Z. Zhou, Y. Hu, Z. Cheng and X. Fang, *Ind. Eng. Chem. Res.*, 2017, **56**, 5802–5812.
17 H. Cui, Q. Zhang, Y. Hu, C. Peng, X. Fang, Z. Cheng, V. V. Galvita and Z. Zhou, *ACS Appl. Mater. Interfaces*, 2018, **10**, 20611–20620.
18 X. Zhao, G. Ji, W. Liu, X. He, E. J. Anthony and M. Zhao, *Chem. Eng. J.*, 2018, **332**, 216–226.
19 V. Hiremath, M. L. T. Trivino and J. G. Seo, *J. Environ. Sci.*, 2019, **76**, 80–88.
20 K. Zhang, X. S. Li, H. Chen, P. Singh and D. L. King, *J. Phys. Chem. C*, 2016, **120**, 1089–1096.
21 K. Wang, Y. Zhao, P. T. Clough, P. Zhao and E. J. Anthony, *Chem. Eng. J.*, 2019, **372**, 886–895.
22 F. Taleshi and A. A. Hosseini, *J. Nanostruct. Chem.*, 2012, **3**, 4.
23 P.-X. Hou, C. Liu and H.-M. Cheng, *Carbon*, 2008, **46**, 2003–2025.
24 N. Buzgar and A. I. Apopei, *Geologie*, 2009, **55**(2), 97–112.
25 A. Weibel, D. Mesguich, G. Chevallier, E. Flahaut and C. Laurent, *Carbon*, 2018, **136**, 270–279.
26 W. Wang, S. Guo, I. Ruiz, M. Ozkan and C. S. Ozkan, *ECS Trans.*, 2013, **50**, 37.
27 J. W. Choi, S. K. Youn and H. G. Park, *J. Nanomater.*, 2013, **2013**, 734686.
28 J. C. Maya, F. Chejne, C. A. Gómez and S. K. Bhatia, *AIChE J.*, 2018, **64**, 3638–3648.
29 A. H. Bork, M. Rekhtina, E. Willinger, P. Castro-Fernández, J. Drnec, P. M. Abdala and C. R. Müller, *Proc. Natl. Acad. Sci. U. S. A.*, 2021, **118**, e2103971118.
30 W. Gao, J. Xiao, Q. Wang, S. Li, M. A. Vasiliades, L. Huang, Y. Gao, Q. Jiang, Y. Niu, B. Zhang, Y. Liu, H. He and A. M. Efstathiou, *Adv. Mater.*, 2022, **34**(4), 2106677.
31 H. Lee, M. L. T. Triviño, S. Hwang, S. H. Kwon, S. G. Lee, J. H. Moon, J. Yoo and J. G. Seo, *ACS Appl. Mater. Interfaces*, 2018, **10**, 2414–2422.
32 P. Chammingkwan, L. T. T. Mai, T. Ikeda and P. Mohan, *J. CO2 Util.*, 2021, **51**, 101652.
33 A. H. Ruhaimi and M. A. Ab Aziz, *J. Solid State Chem.*, 2021, **300**, 122242.